Transition strengths and band terminations in ^{86}Zr

M. Wiedeking,[1] S. L. Tabor,[1] F. Cristancho,[2] M. Devlin,[3] J. Döring,[4,*] C. B. Jackson,[1] G. D. Johns,[5] R. A. Kaye,[1,†] I. Y. Lee,[6] F. Lerma,[3] A. O. Macchiavelli,[6] M. Naidu,[1] I. Ragnarsson,[7] D. G. Sarantites,[3] and G. Z. Solomon[1]

[1]*Department of Physics, Florida State University, Tallahassee, Florida 32306*

[2]*Departamento de Física, Universidad Nacional de Colombia, Bogotá, Colombia*

[3]*Chemistry Department, Washington University, St. Louis, Missouri 63130*

[4]*Department of Physics, University of Notre Dame, Notre Dame, Indiana 46556*

[5]*Los Alamos National Laboratory, Los Alamos, New Mexico 87545*

[6]*Nuclear Science Division, Lawrence Berkeley National Laboratory, Berkeley, California 94720*

[7]*Department of Mathematical Physics, Lund Institute of Technology, S-21100 Lund, Sweden*

(Received 19 November 2002; published 31 March 2003)

High angular momentum states in ^{86}Zr were populated through the ^{58}Ni(^{32}S,4p) reaction at 135 MeV using the 88-In. Cyclotron at Lawrence Berkeley National Laboratory. Recoiling ^{86}Zr nuclei were stopped in a thick Ta backing. Prompt multi-γ coincidences with evaporated charged particles were detected using the full array of GAMMASPHERE and the MICROBALL. Mean lifetimes of 36 levels in ^{86}Zr were measured using the Doppler-shift attenuation method. Transition quadrupole moments Q_t were found in the range of about 0.3–1.5 e b in the positive-parity bands. The negative-parity bands show Q_t values from about 0.25 to 1.2 e b. In the yrast positive-parity band, a sharp drop in collectivity approaching the 30^+ state supports the interpretation of band termination in this configuration. Decreasing Q_t values approaching the 24^+ and 27^- states also provide an indication of terminating structures.

DOI: 10.1103/PhysRevC.67.034320 PACS number(s): 21.10.Ky, 21.10.Tg, 23.20.−g, 27.50.+e

I. INTRODUCTION

Nuclei in the f-p-g shell exhibit a wide and rapidly changing range of shapes, with structures ranging from highly collective to single particle. As a result, the nuclei in this mass region provide an excellent laboratory for studying the interaction between single-particle and collective degrees of freedom.

The Zr isotopes ($Z=40$) form one of the best examples, with shapes varying from highly deformed ^{80}Zr to spherical ^{90}Zr at the $N=50$ shell closure. Near the middle of the range, ^{86}Zr is clearly transitional in structure and shape, even though a superdeformed band has been observed in this nucleus [1]. Sequences of states appear to form regular rotational bands interrupted by different level spacings indicative of structural changes. This tightly interwoven pattern of single-particle and collective features has led to challenges in understanding ^{86}Zr. Recently, the structural changes at high spin were observed and interpreted as band terminations reflecting the underlying single-particle structure [2]. This was based on the good agreement between the level energies and calculations performed within the configuration-dependent shell-correction approach using a cranked Nilsson potential [3]. Clearly, transition strengths would provide more information on possible band terminations.

Several investigations [4–7] had been performed on the level structure of ^{86}Zr prior to the work reported in Ref. [2]. A number of g-factor measurements were made [8–10] to study the quasiparticle structure of the bands. Previous lifetime measurements [4,6,7,11] have extended the range of known lifetimes up to the 13^- and 24^+ states. In order to further test the band termination picture, it is necessary to know the lifetimes up to the 27^- and 30^+ states. This was achieved in the present work using GAMMASPHERE [12] and the MICROBALL [13] detector systems. Particle and multiple-γ gating provided cleaner line shapes than previously possible. The higher statistics allowed gating from above to eliminate the uncertainties of side feeding from many of the line shapes.

II. EXPERIMENTAL PROCEDURE

High-spin states in ^{86}Zr were populated using the reaction ^{58}Ni(^{32}S,4p) at 135 MeV with beams from the 88-in. Cyclotron at Lawrence Berkeley National Laboratory. The experiment was optimized for lifetime measurements using the Doppler-shift attenuation method (DSAM) with a 415 μg/cm^2-thick ^{58}Ni target evaporated on a 10.3 mg/cm^2 Ta backing. γ rays from the reactions were detected with GAMMASPHERE. The evaporated charged particles were detected and identified with the MICROBALL. The experimental procedure is described in more detail in Ref. [14].

For the DSAM analysis, the data were sorted into different 3000×3000 channel square matrices. To obtain optimum selection of ^{86}Zr events, all matrices were gated on the requirement of three or four protons detected in the MICROBALL. The matrices were also gated on the requirement of an additional coincident γ ray. To select the positive-

*Present address: GSI, 64291 Darmstadt, Germany.

†Present address: Department of Chemistry and Physics, Purdue University Calumet, Hammond, IN 46323.

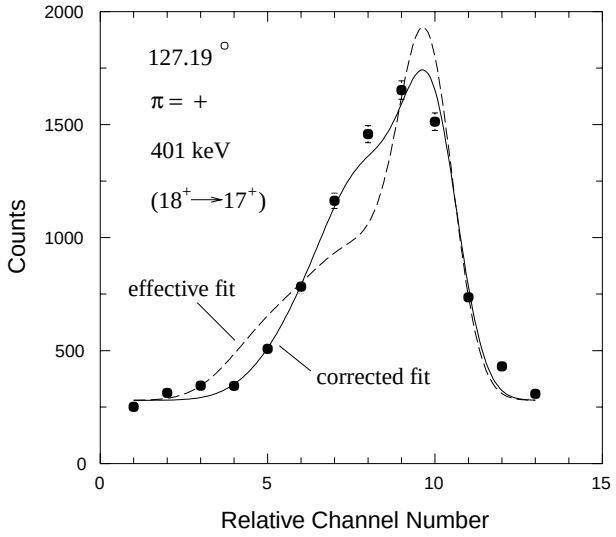

FIG. 1. A comparison of the best fits with (solid line) and without (dashed line) correction for direct feeding for the 401 keV line shape (band 2) gated from above. Unless otherwise noted, the dispersion is 1.33 keV/channel on the line shape graphs.

parity bands this additional γ ray was required to be one of the following lines: 234, 628, 886, 915, 925, 978, 1003, or 1027 keV. Separate matrices were sorted to enhance the negative-parity bands by requiring either the 234, 628, 886, 915, 1003, 1006, 1008, 815, 718, or 1039 keV lines as the additional coincident γ ray.

γ rays from any of the detectors were sorted onto one axis of the square matrices to allow for a second γ gate in selecting the line shapes. Only lines from detectors at approximately the same θ angle were sorted onto the second axis, from which the line shapes to be fitted were obtained. Pairs of detector rings were combined yielding weighted average angles of 34.95° (seven active detectors), 52.81° (15 active detectors), 127.19° (15 active detectors), and 145.45° (ten active detectors). The reliability of this approximation was verified in Ref. [14].

III. LIFETIME MEASUREMENTS

Mean lifetimes for the shorter-lived, higher-lying states in all bands were analyzed by applying the Doppler-shift at-

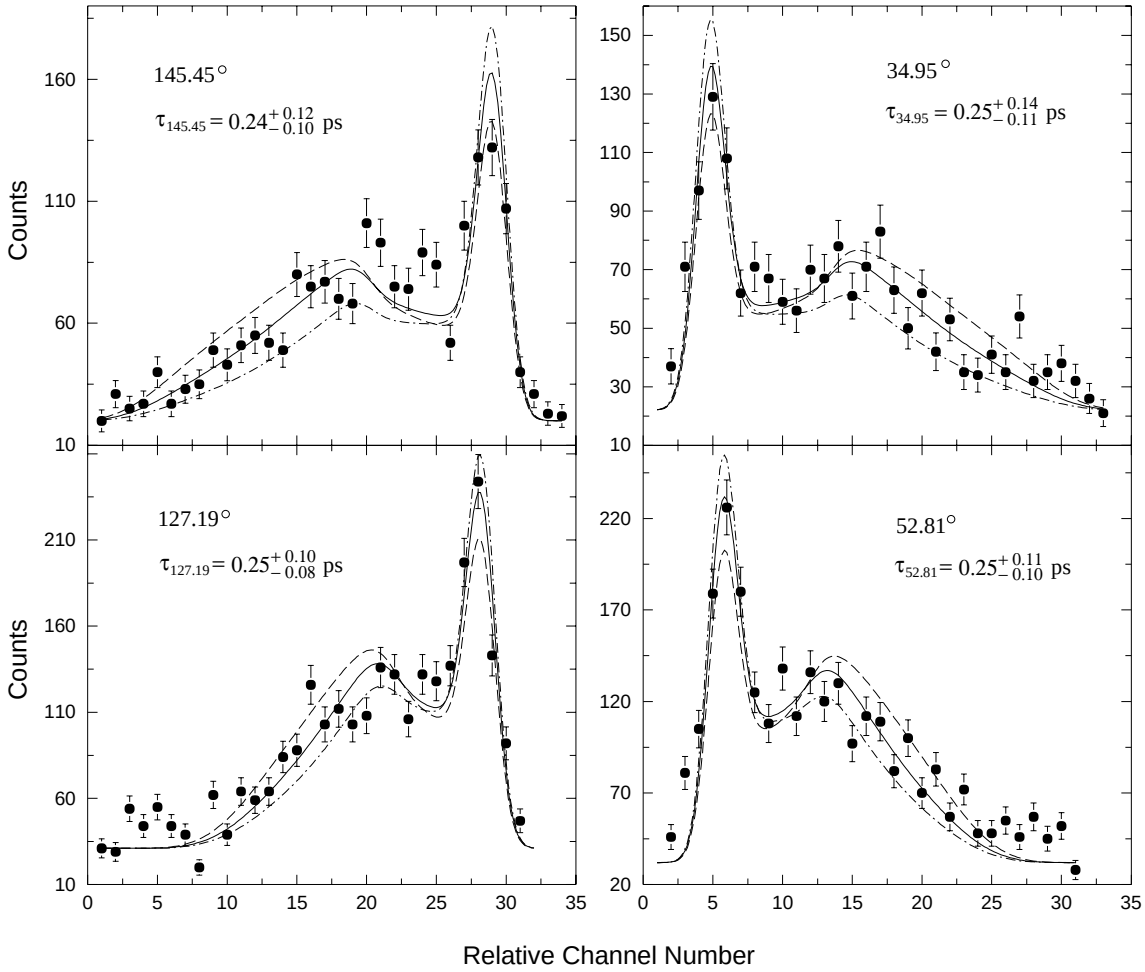

FIG. 2. The 1305 keV transition ($19^- \rightarrow 17^-$, band 5) fitted individually at all four angles. Fits representing the uncertainty limits are shown with dashed and dot-dashed lines.

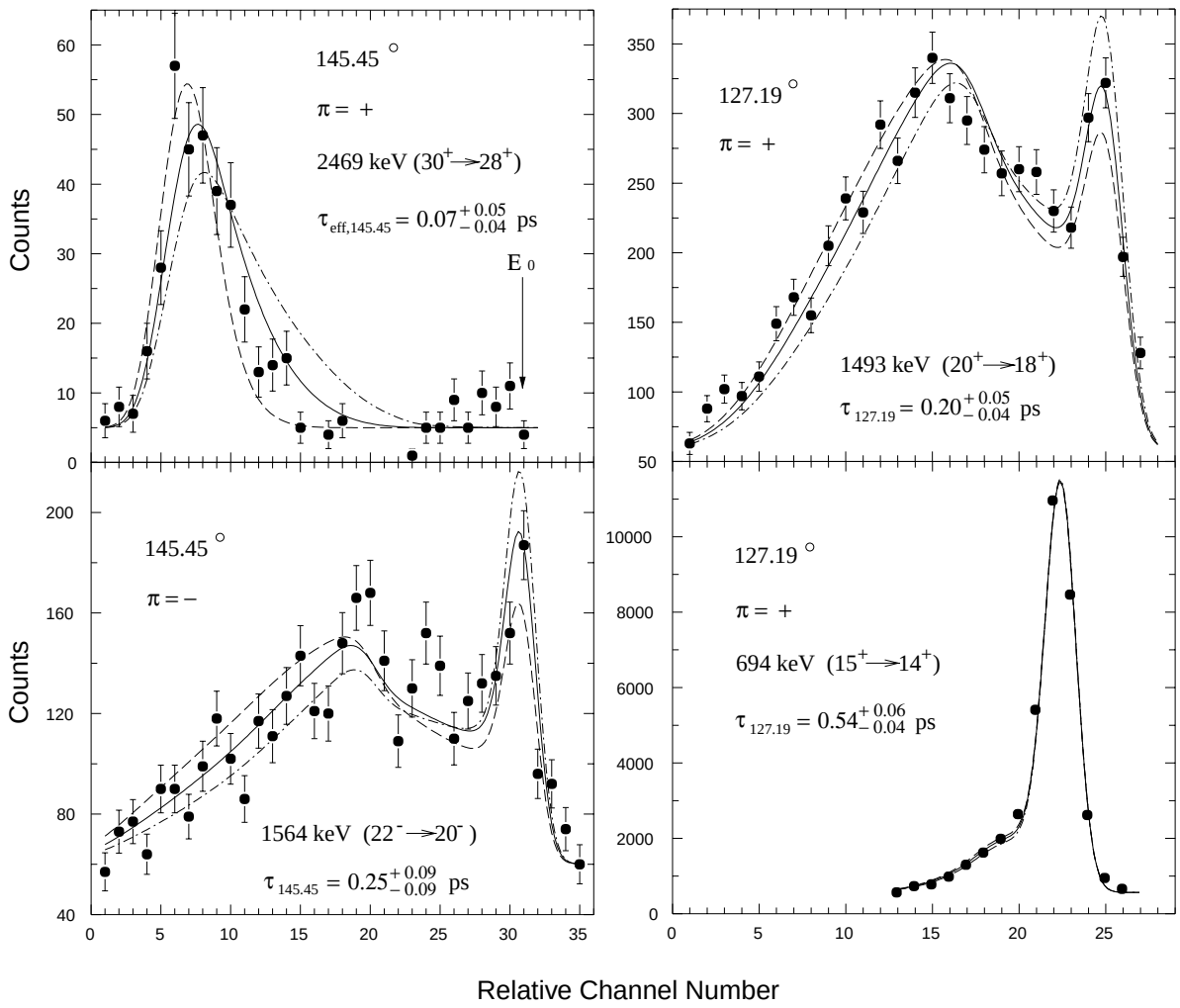

FIG. 3. A sample of line shape fits over the range of lifetimes measured. The best fits are shown with solid lines, while the dashed and dot-dashed lines represent the uncertainty limits. The dispersion is 1.33 keV/channel as in all the other line shape figures, except for the 2469 keV graph, whose dispersion is 2.67 keV/channel.

tenuation method to the experimental line shapes. The decay times of the recoiling nuclei were compared with their slowing-down times in the target and backing material using the computer simulation code FITS [15] that integrates over the thickness of the target and determines the distribution of recoil velocities as the nuclei slow down and decay. The required stopping powers were calculated using SRIM version 2000.10 [16,17]. In addition the program corrects for feeding from both known and unknown higher-lying states as well as for finite detector solid angle and resolution and for the energy dependence of the reaction cross sections as the beam decelerates through the target.

The theoretical line shapes generated by FITS for a range of possible mean lifetimes were compared to the coincidence spectra at each of the four angles, 34.95°, 52.81°, 127.19°, and 145.45°. The lifetimes giving the best fit (lowest χ^2) were determined separately for each angle of observation. The uncertainty of each individual lifetime was determined by finding the lifetime value above and below the best fit value at which χ^2 increases by one unit. The weighted average of the lifetimes from the individual angles was calculated to determine the accepted values. The uncertainties for the accepted lifetimes were calculated from the pooled (unweighted) and weighted variances (whichever was larger) and include estimates for contributions from the stopping powers.

Each line shape was first fitted with no feeding correction to determine the effective lifetime, which represents an upper limit for the lifetime of the state. Each transition, except for the highest one in each cascade with adequate statistics for fitting, was fitted again, taking direct (known) feeding and side (unknown) feeding into account. The direct feeding correction used the effective lifetime of the state or states immediately above, and the lifetimes were varied until the best fit was obtained. Figure 1 shows the effect of feeding corrections for the 401 keV line shape.

Whenever possible, lifetimes of the transitions were determined by fitting line shapes obtained by gating from

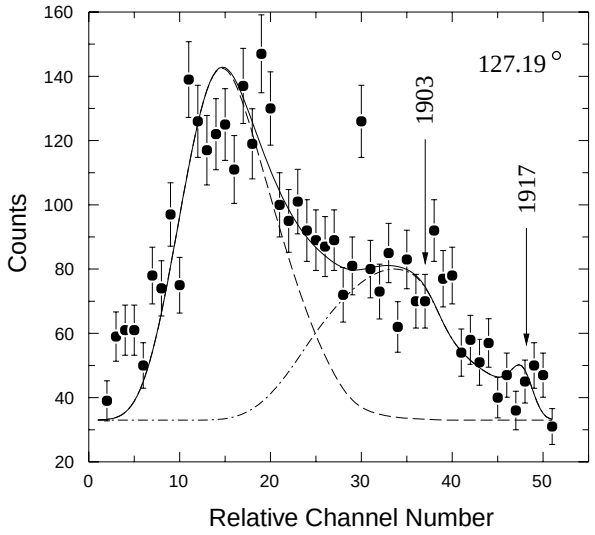

FIG. 4. An illustration of simultaneous fits to the 1903 ($26^+ \rightarrow 24^+$, band 1) and 1917 keV ($22^+ \rightarrow 20^+$, band 2) line shapes gated from above. The dashed (dot-dashed) line shows the simulation for the 1903 keV (1917 keV) line shape only. The solid line, representing the sum of the individual line shapes, was fitted to the data. The arrows indicate the positions of the unshifted peaks.

above (GFA) the transition of interest to eliminate the contribution of side feeding. This was made possible by applying an approximate Doppler-shift correction before gating on the 2469, 2013, 2088, 1903, or 1917 keV ($\pi = +$) or 2240 keV ($\pi = -$) transitions. In all cases the line shapes gated from below (GFB) the transition of interest were also fitted. In the cases where the lifetime was determined from the GFA line shape, that lifetime was held constant while the side-feeding time was varied to fit the GFB line shape. The side-feeding times determined from this comparison averaged 30% of the effective lifetimes extracted from the line shapes directly above the transition of interest. This is rather similar to the ratio of 35% found for ^{86}Nb in the same experiment [14]. The 30% ratio was then used to estimate the side feeding times for line shapes which could not be gated from above.

The line shapes of the 1305 keV transition in a negative-parity band are shown at all four angles in Fig. 2 as an example of the variation with angle. Figure 3 illustrates the variation of the line shapes from the shortest to one of the longest lifetimes measured.

In most cases it was possible to fit each transition individually, without interference from other peaks, by a judicious choice of gates. Where this was not possible, a modified version of FITS was used to fit two overlapping line shapes simultaneously, by comparison with the properly scaled sum of the two theoretical line shapes. Figure 4 shows an example for the 1903 and 1917 keV lines in the yrast band. This method proved very reliable, as shown in Ref. [14].

IV. RESULTS

A. Lifetimes

To facilitate the discussion, the level scheme of ^{86}Zr adapted from Ref. [2] is shown in Fig. 5. The band structure has been rearranged slightly based on the present results, and bands have been numbered for the discussion. The lifetimes measured in the present work are listed in Table I. Table II lists and compares all lifetimes published to date. The most recent lifetime for the 3298 keV 8^+ state was adopted because previously unknown β-decay feeding may have affected the earlier measurements, as discussed in Ref. [11]. Accepted mean lifetimes were used for all $B(M1)$ and $B(E2)$ calculations in this work.

In order to get very good statistical results in the positive- and negative-parity bands it was generally sufficient to use only individual gates or very few gates to reduce contamination from other γ rays. However, it was necessary to add more gates together to obtain adequate statistics in the weak sidebands.

The highest-lying positive-parity states for which line shapes could be extracted and lifetimes determined were the 20 532 keV (30^+, band 1), and 9652 keV (18^+, band 4) levels; thus only effective lifetimes are quoted for these states. It was not possible to separate the 1903 and 1917 keV line shapes (bands 1 and 2) because of their cascade relationship, so it was necessary to fit their combined line shape using the modified version of FITS. No reliable lifetime could be extracted for the 1400 keV transition.

The highest-lying negative-parity state which could be analyzed in the present work was the 16 616 keV (27^-, band 5) level. It was not possible to extract reliable lifetimes for the 1806 (band 6) and 1201 keV (band 8) transitions. To feeding correct the 1564 keV line (band 6), the 1806 keV intensity of 2.0 (normalized with respect to the 752 keV line) was added to the larger 381 keV intensity of 3.3 and the effective lifetime of the 1509 keV line was used for the entire direct feeding. The 1644 keV line shape was fitted together with the 1634 keV (band 5) one where the latter one's lifetime was fixed to the measured lifetime given in Table I.

Eight of the lifetimes in the yrast band measured in the present work had been measured previously [7]. There is good agreement in half the cases. The differences in the lifetimes of the 10 142 keV 20^+ and 9890 keV 19^+ states may be due to interference of the 1634, 1644, 1632, 1508, and 1509 keV lines with fits to the 1643 and 1493 keV line shapes. The interfering lines [2] were not known at the time of Ref. [7] and were carefully removed by selective gating in the present analysis. The longer lifetimes of the 15^+ and 16^+ states lead to weaker Doppler-shifted components and greater sensitivity to background contamination. The use of GAMMASPHERE and the MICROBALL allowed more thorough gating to provide cleaner line shapes. A fit to the 694 keV line shape from the 15^+ state is shown in Fig. 3. The 1075 keV line shape is shown in Fig. 6 along with theoretical curves for the present fit of 0.46 ps and the previous value of 0.85 ps.

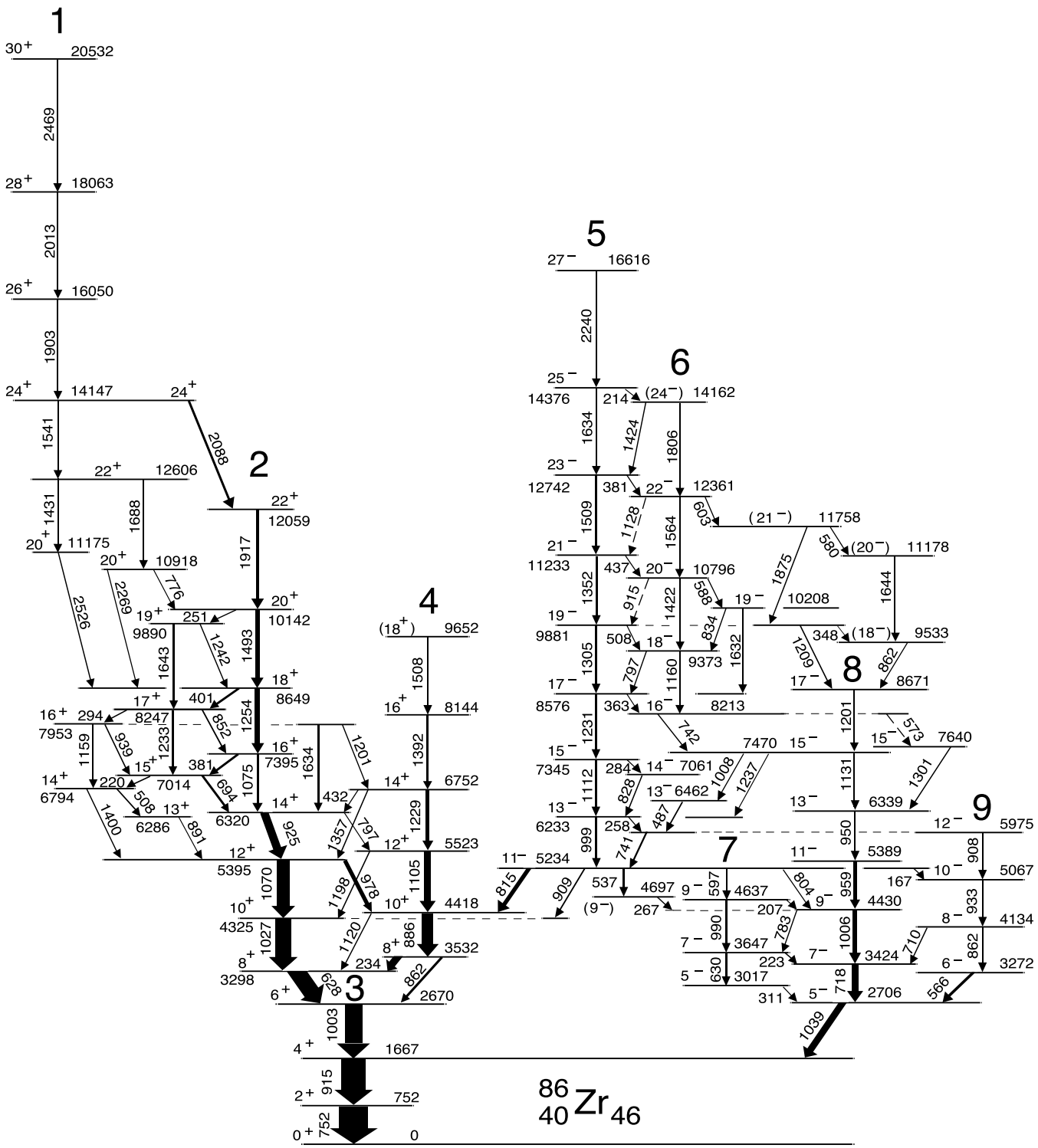

FIG. 5. The level scheme of ^{86}Zr as deduced from Ref. [2] and the present work. The arbitrary numbers above the decay sequences are intended only to facilitate the discussion.

B. Transition strengths

The electric quadrupole transition strengths $B(E2)$ were determined from the accepted lifetimes, transition energies [2], and branching ratios (deduced from the data of Ref. [2]) given in Tables I and II and were used to calculate transition quadrupole moments $|Q_t|$ from the rotational model. A value of $K=0$ was used for all bands. K values of 3 and 5 were tested in calculating Q_t values in the negative-parity bands. The different K values had no significant effect for the states above 7^-. However, the Q_t values for the 7^- states were unreasonably large for $K=3$ and 5, suggesting that the effective K value is lower. Therefore, $K=0$ was used. Both

TABLE I. Level energies, spins of initial and final states, γ-ray energies, relative intensities, effective lifetimes, mean lifetimes at each angle and the accepted mean lifetimes in ^{86}Zr. Lifetimes were measured by gating on the transition above the one of interest except where noted. The effective and accepted lifetimes are the weighted average of all possible angles. Energies and spin assignments were taken from Ref. [2]. The relative intensities (deduced from the data of Ref. [2]) are normalized relative to 100 for the 752 keV line.

E_x	I_i^π	I_f^π	E_γ	I_γ	τ_{eff} [a]	τ (ps)				τ_{acc}
(keV)			(keV)		(ps)	34.95°	52.81°	127.19°	145.45°	(ps)
					$\pi = +$					
20532	30^+	28^+	2469	2.3(2)	$0.06^{+0.02}_{-0.02}$ [b]					
18063	28^+	26^+	2013	3.6(2)	$0.13^{+0.02}_{-0.02}$	$0.05^{+0.03}_{-0.03}$	$0.08^{+0.03}_{-0.03}$	$0.07^{+0.06}_{-0.05}$	$0.07^{+0.04}_{-0.03}$	$0.07^{+0.02}_{-0.02}$ [b]
16050	26^+	24^+	1903	5.2(3)	$0.19^{+0.03}_{-0.03}$	$0.04^{+0.05}_{-0.03}$	$0.03^{+0.04}_{-0.02}$	$0.03^{+0.02}_{-0.02}$	$0.05^{+0.03}_{-0.02}$	$0.04^{+0.02}_{-0.01}$
14147	24^+	22^+	2088	2.9(2)	$0.26^{+0.04}_{-0.03}$	$0.06^{+0.04}_{-0.03}$	$0.06^{+0.05}_{-0.03}$	$0.08^{+0.06}_{-0.05}$	$0.10^{+0.04}_{-0.03}$	$0.08^{+0.02}_{-0.02}$ [b]
12606	22^+	20^+	1431	2.7(3)	$0.41^{+0.08}_{-0.07}$ [c]		$0.09^{+0.07}_{-0.05}$	$0.17^{+0.06}_{-0.05}$		$0.18^{+0.07}_{-0.07}$ [b c]
		20^+	1688	2.2(2)	$0.41^{+0.08}_{-0.07}$ [c]	$0.20^{+0.13}_{-0.10}$	$0.20^{+0.12}_{-0.09}$	$0.27^{+0.07}_{-0.08}$	$0.31^{+0.11}_{-0.09}$	$0.18^{+0.07}_{-0.07}$ [b c]
12059	22^+	20^+	1917	6.0(3)	$0.40^{+0.05}_{-0.04}$	$0.11^{+0.07}_{-0.05}$	$0.04^{+0.06}_{-0.03}$	$0.11^{+0.04}_{-0.04}$	$0.14^{+0.08}_{-0.06}$	$0.09^{+0.03}_{-0.04}$
11175	20^+	18^+	2526	2.2(4)	$0.35^{+0.06}_{-0.05}$			$0.06^{+0.07}_{-0.05}$	$0.07^{+0.06}_{-0.05}$	$0.07^{+0.05}_{-0.04}$ [b]
10918	20^+	18^+	2269	3.1(4)	$0.48^{+0.09}_{-0.08}$		$0.13^{+0.15}_{-0.12}$	$0.16^{+0.09}_{-0.08}$		$0.15^{+0.08}_{-0.07}$ [b]
10142	20^+	18^+	1493	9.8(5)	$0.67^{+0.07}_{-0.06}$	$0.19^{+0.04}_{-0.05}$	$0.18^{+0.05}_{-0.04}$	$0.20^{+0.05}_{-0.04}$	$0.19^{+0.05}_{-0.05}$	$0.19^{+0.02}_{-0.02}$
9890	19^+	17^+	1643	3.0(4)	$0.65^{+0.04}_{-0.04}$	$0.37^{+0.09}_{-0.09}$	$0.30^{+0.06}_{-0.05}$	$0.36^{+0.07}_{-0.08}$	$0.33^{+0.09}_{-0.07}$	$0.33^{+0.04}_{-0.03}$ [b]
9652	(18^+)	16^+	1508	1.8(2)	$0.54^{+0.13}_{-0.11}$ [b]					
8649	18^+	16^+	1254	7.3(3)	$1.17^{+0.13}_{-0.13}$ [c]	$0.31^{+0.10}_{-0.08}$	$0.30^{+0.07}_{-0.05}$			$0.29^{+0.02}_{-0.02}$ [c]
		17^+	401	6.2(3)	$1.17^{+0.13}_{-0.13}$ [c]	$0.28^{+0.09}_{-0.08}$	$0.29^{+0.04}_{-0.05}$	$0.27^{+0.04}_{-0.04}$	$0.32^{+0.06}_{-0.05}$	$0.29^{+0.02}_{-0.02}$ [c]
8247	17^+	16^+	852	7.0(4)	$1.46^{+0.24}_{-0.24}$			$0.29^{+0.04}_{-0.04}$	$0.26^{+0.06}_{-0.05}$	$0.28^{+0.03}_{-0.03}$
8144	16^+	14^+	1392	2.8(2)	$0.75^{+0.17}_{-0.11}$	$0.30^{+0.23}_{-0.16}$	$0.30^{+0.27}_{-0.19}$	$0.35^{+0.22}_{-0.16}$	$0.22^{+0.17}_{-0.12}$	$0.28^{+0.11}_{-0.08}$
7953	16^+	14^+	1634	2.2(3)	$1.05^{+0.24}_{-0.16}$	$0.89^{+0.43}_{-0.14}$	$0.60^{+0.29}_{-0.22}$	$0.86^{+0.64}_{-0.27}$	$0.90^{+0.80}_{-0.30}$	$0.76^{+0.22}_{-0.13}$
7395	16^+	14^+	1075	6.3(3)	$1.73^{+0.20}_{-0.16}$	$0.48^{+0.14}_{-0.10}$	$0.46^{+0.11}_{-0.10}$	$0.48^{+0.22}_{-0.17}$	$0.62^{+0.50}_{-0.21}$	$0.48^{+0.08}_{-0.06}$ [b]
7014	15^+	14^+	694	18.3(7)	$4.05^{+0.40}_{-0.45}$	$0.78^{+0.14}_{-0.12}$	$0.76^{+0.07}_{-0.06}$	$0.54^{+0.06}_{-0.04}$	$0.47^{+0.06}_{-0.05}$	$0.58^{+0.12}_{-0.11}$
6752	14^+	12^+	1229	11.0(9)	$1.99^{+0.34}_{-0.33}$	$0.54^{+0.36}_{-0.19}$	$0.60^{+0.21}_{-0.13}$	$0.41^{+0.14}_{-0.10}$	$0.39^{+0.16}_{-0.12}$	$0.45^{+0.09}_{-0.09}$
6286	13^+	12^+	891	2.8(2)	$1.70^{+0.31}_{-0.30}$		$0.62^{+0.20}_{-0.27}$	$0.99^{+0.31}_{-0.21}$		$0.79^{+0.18}_{-0.19}$ [b]
5523	12^+	10^+	1198	6.5(4)	$2.68^{+0.37}_{-0.33}$	$0.63^{+0.61}_{-0.28}$	$0.42^{+0.22}_{-0.15}$	$0.62^{+0.32}_{-0.20}$	$0.46^{+0.31}_{-0.20}$	$0.49^{+0.15}_{-0.10}$ [b]
					$\pi = -$					
16616	27^-	25^-	2240	3.2(2)	$0.12^{+0.05}_{-0.03}$ [b]					
14376	25^-	23^-	1634	5.7(3)	$0.46^{+0.07}_{-0.06}$	$0.33^{+0.16}_{-0.14}$	$0.40^{+0.14}_{-0.12}$	$0.39^{+0.13}_{-0.12}$	$0.42^{+0.16}_{-0.13}$	$0.39^{+0.07}_{-0.06}$
12742	23^-	21^-	1509	8.1(4)	$0.73^{+0.07}_{-0.07}$	$0.27^{+0.06}_{-0.05}$	$0.27^{+0.12}_{-0.09}$	$0.16^{+0.18}_{-0.16}$	$0.11^{+0.12}_{-0.09}$	$0.24^{+0.06}_{-0.06}$
12361	22^-	20^-	1564	4.1(2)	$0.73^{+0.07}_{-0.07}$ [c]	$0.25^{+0.08}_{-0.07}$	$0.31^{+0.07}_{-0.06}$	$0.27^{+0.06}_{-0.09}$	$0.25^{+0.09}_{-0.09}$	$0.26^{+0.03}_{-0.03}$ [c]
		(21^-)	603	3.4(2)	$0.73^{+0.07}_{-0.07}$ [c]	$0.21^{+0.09}_{-0.07}$	$0.25^{+0.06}_{-0.05}$			$0.26^{+0.03}_{-0.03}$ [c]
11758	(21^-)	19^-	1875	2.2(4)	$0.86^{+0.19}_{-0.19}$		$0.11^{+0.12}_{-0.09}$	$0.23^{+0.14}_{-0.10}$		$0.16^{+0.09}_{-0.07}$
11233	21^-	19^-	1352	6.6(3)	$0.67^{+0.09}_{-0.06}$	$0.33^{+0.13}_{-0.11}$	$0.32^{+0.12}_{-0.10}$	$0.40^{+0.13}_{-0.11}$	$0.30^{+0.13}_{-0.10}$	$0.34^{+0.06}_{-0.05}$ [b]
11178	(20^-)	(18^-)	1644	3.3(4)	$1.19^{+0.39}_{-0.31}$	$0.29^{+0.35}_{-0.21}$	$0.38^{+0.36}_{-0.28}$			$0.33^{+0.25}_{-0.17}$
10796	20^-	18^-	1422	2.6(3)	$0.81^{+0.09}_{-0.08}$	$0.20^{+0.12}_{-0.10}$	$0.24^{+0.13}_{-0.15}$	$0.22^{+0.15}_{-0.17}$	$0.20^{+0.13}_{-0.17}$	$0.21^{+0.07}_{-0.07}$
10208	19^-	18^-	834	4.6(3)	$1.46^{+0.28}_{-0.21}$		$0.49^{+0.13}_{-0.09}$		$0.45^{+0.16}_{-0.11}$	$0.47^{+0.10}_{-0.07}$
9881	19^-	17^-	1305	6.7(4)	$0.91^{+0.10}_{-0.06}$	$0.25^{+0.14}_{-0.11}$	$0.25^{+0.11}_{-0.10}$	$0.25^{+0.10}_{-0.08}$	$0.24^{+0.12}_{-0.10}$	$0.25^{+0.06}_{-0.05}$ [b]
9533	(18^-)	17^-	862	5.5(3)	$1.75^{+0.58}_{-0.27}$	$0.45^{+0.40}_{-0.24}$	$0.57^{+0.93}_{-0.27}$	$0.45^{+0.33}_{-0.21}$	$0.79^{+0.95}_{-0.37}$	$0.49^{+0.24}_{-0.13}$
9373	18^-	17^-	797	7.7(4)	$1.75^{+0.47}_{-0.26}$			$0.47^{+0.20}_{-0.14}$	$0.47^{+0.28}_{-0.19}$	$0.47^{+0.16}_{-0.11}$
8576	17^-	15^-	1231	12.6(7)	$2.71^{+0.19}_{-0.21}$	$0.89^{+0.19}_{-0.14}$	$0.94^{+0.16}_{-0.19}$	$1.05^{+0.19}_{-0.11}$	$0.99^{+0.18}_{-0.14}$	$0.97^{+0.09}_{-0.07}$ [b]
8213	16^-	15^-	742	8.8(5)	$3.92^{+0.57}_{-0.60}$			$0.35^{+0.09}_{-0.08}$	$0.28^{+0.12}_{-0.09}$	$0.32^{+0.07}_{-0.06}$
7640	15^-	13^-	1301	2.2(2)	$1.77^{+0.28}_{-0.17}$ [b]					
7470	15^-	13^-	1131	3.9(4)	$3.11^{+0.38}_{-0.64}$	$0.74^{+0.36}_{-0.23}$	$1.07^{+0.49}_{-0.29}$	$1.17^{+0.61}_{-0.34}$	$0.95^{+0.57}_{-0.31}$	$0.93^{+0.24}_{-0.17}$ [b]

[a] Weighted average of effective lifetimes measured at all possible angles.

[b] Gated from below (GFB).

[c] τ_{eff} and τ_{acc} are determined by the weighted average of all available values for both transitions.

TABLE II. Comparison of mean lifetimes measured in previous and current work.

E_x (keV)	I_i^π	τ [a] (ps)	τ [b] (ps)	τ [c] (ps)	τ [d] (ps)	$\tau_{present}$ (ps)	$\tau_{accepted}$ (ps)
				$\pi=+$			
14147	24^+			$0.09^{+0.12}_{-0.06}$		$0.08^{+0.02}_{-0.02}$	$0.08^{+0.02}_{-0.02}$
12059	22^+			$0.08^{+0.10}_{-0.05}$		$0.09^{+0.03}_{-0.04}$	$0.09^{+0.03}_{-0.04}$
10142	20^+			$0.40^{+0.12}_{-0.05}$		$0.19^{+0.02}_{-0.02}$	$0.19^{+0.02}_{-0.02}$
9890	19^+			$0.10^{+0.12}_{-0.03}$		$0.33^{+0.04}_{-0.03}$	$0.33^{+0.04}_{-0.03}$
8649	18^+			$0.33^{+0.07}_{-0.03}$		$0.29^{+0.02}_{-0.02}$	$0.29^{+0.02}_{-0.02}$
8247	17^+			$0.22^{+0.15}_{-0.03}$		$0.28^{+0.03}_{-0.03}$	$0.28^{+0.03}_{-0.03}$
7395	16^+		<1.5	$0.85^{+0.20}_{-0.03}$		$0.48^{+0.08}_{-0.06}$	$0.48^{+0.08}_{-0.06}$
7014	15^+		<1.0	$0.80^{+0.20}_{-0.03}$		$0.58^{+0.12}_{-0.11}$	$0.58^{+0.12}_{-0.11}$
6320	14^+		7.5(9)				7.5(9)
5395	12^+		3.8(9)		5(2) [e]		3.8(9)
4418	10^+		13(4)		11(4) [e]		12(3)
4325	10^+		3.0(6)		3.2(10)		3.1(5)
3532	8^+		<5		4.7(10)		4.7(10)
3298	8^+	90(9)	90(10)		67(8)		67(8)
2670	6^+	11.5(52)			12.2(49)		11.9(36)
1667	4^+	8.7(39)			7.8(34)		8.2(26)
752	2^+	10.6(20)			11.2(28)		10.8(16)
				$\pi=-$			
6233	13^-		6.1(10)				6.1(10)
5975	12^-		<2				<2
5389	11^-		4(1)				4(1)
5234	11^-		18(8)				18(8)
4430	9^-		11(2)		11(4) [e]		11(2)
3647	7^-		<10				<10
3424	7^-		12(2)		7.7(30)		10.7(17)
3017	5^-		<20				<20
2706	5^-		<100		20(10) [e]		<20

[a]Reference [4].
[b]Reference [6].
[c]Reference [7].
[d]Reference [11].
[e]Effective lifetime.

quantities $B(E2)$ and the transition quadrupole moments Q_t are given in Table III.

Magnetic dipole transition strengths $B(M1)$ were calculated using a quadrupole-dipole mixing ratio of $\delta=0$, since $B(M1)$ values are rather insensitive to δ as long as it is small. The magnetic dipole transition strengths for the positive- and negative-parity bands are given in Tables IV and V, respectively.

Although the lifetimes of the states below about 14^+ and 15^- are too long to be measured with the DSAM, Q_t, $B(E2)$, and $B(M1)$ values were calculated using lifetimes measured in previous work [4,6,11] for completeness.

V. DISCUSSION

A. Positive-parity bands

Graphs of spin I, kinematic $J^{(1)}$, and dynamic $J^{(2)}$ moments of inertia as functions of rotational frequency ω are shown in Fig. 7 for the positive-parity bands. The $J^{(2)}$ values show reasonably good rotational behavior for rotational frequencies above 0.5 MeV/$\hbar$, especially for band 2. The graphs also show several changes in structure in the positive-parity bands. The first change occurs at the 8^+ states. The yrast 8^+ state has been interpreted as involving a $g_{9/2}$ neutron alignment on the basis of the small or negative g factor [8–10]. A g factor larger than the rotational value suggests a quasiproton configuration for the 8_2^+ state [9] in band 4. An increase in the g factor is observed in the yrast band above the second discontinuity at the 12_1^+ state. Since four quasiparticles are energetically allowed at this energy, a configuration involving both aligned neutron and proton pairs has been suggested as most likely [9].

Calculations with the configuration-dependent cranked Nilsson-Strutinsky (CNS) approach [3,18] have been performed using the Nilsson potential with the single-particle parameters taken from Ref. [19]. These are the parameters

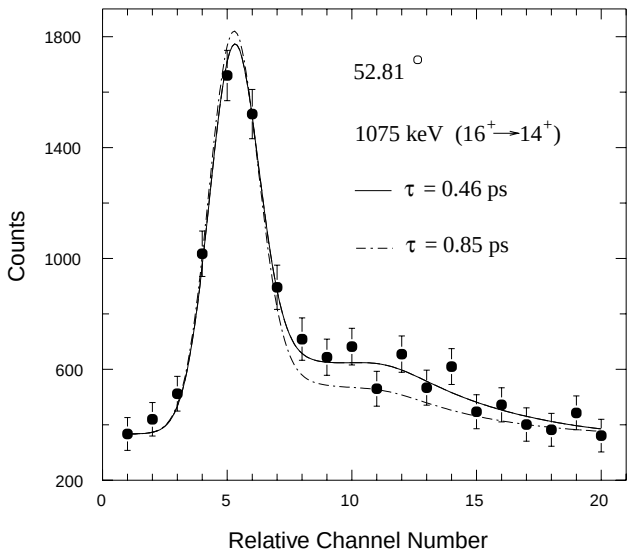

FIG. 6. A comparison of line shapes calculated with the present lifetime of $\tau = 0.46$ ps and a previously reported value [7] of $\tau = 0.85$ ps with the measured data for the 1075 keV transition (band 2) at 52.81°.

which have been used in most calculations in the $A \approx 80$ region, see, e.g., Refs. [18,20]. Comparing with Ref. [2] where somewhat different parameters were used, it turns out that the band structure is very similar. However, the relative energies of the bands might vary by a few hundred keV in the two calculations. The discontinuity above the 24^+ state was observed in Ref. [2] and interpreted as an unpaired crossing. In the calculations, the $[2,6]^+$ configuration (two $g_{9/2}$ protons and six $g_{9/2}$ neutrons) can represent the yrast band up to its termination at the 24^+ state. Above this, the more collective $[4,6]^+$ configuration (with two more $g_{9/2}$ protons and two extra f-p holes) becomes yrast. The graphs in the top panel of Fig. 7 show discrete increases in spin with each structure change, consistent with the interpretation that an increasing number of $g_{9/2}$ particles are involved in these configurations.

To examine the evidence provided by the lifetimes, the transition quadrupole moments Q_t inferred from the measured lifetimes in the positive-parity bands are graphed in the top panel of Fig. 8 as a function of spin. They average about 1 e b, but vary considerably from state to state. For comparison, the experimental level energies minus a rigid rotor reference [2] are graphed in the middle panel of Fig. 8. In the lower panel of the same figure the assigned theoretical configurations are graphed. Clearly, there is a qualitative similarity between the changes in slope of the yrast band in the top and middle graphs. Two band crossings at $12\hbar$ and $18\hbar$ (Fig. 8 bottom) are predicted which correlate with two changes in slope in the experimental level energies (Fig. 8 middle). Also the calculations imply a steep increase in energy cost per spin unit above $18\hbar$ in the $[2,8]^+$ configuration and below $18\hbar$ in the $[4,6]^+$ one. These energetically unfavored states were not observed experimentally. It should be noted that the CNS calculations have to be considered with caution at low spins, since pairing has not been taken into account.

As mentioned above, the slope changes in the energy graph were interpreted in Ref. [2] as evidence of band termination. Now the Q_t values provide more information concerning band terminations. The $[2,6]^+$ configuration, likely to correspond to band 2, becomes fully aligned and terminates at $24\hbar$. The much smaller Q_t value for the 2088 keV $24^+ \rightarrow 22^+$ transition may represent the reduction of collectivity approaching band termination or it may signify a weak interband transition. In the latter case, the 24^+ experimental state would already be a member of the more collective, higher seniority, $[4,6]^+$ configuration. In either case the states above the termination of the $[2,6]^+$ configuration at 24^+ (band 1) must arise from the $[4,6]^+$ configuration. The larger Q_t value of the $26^+ \rightarrow 24^+$ transition confirms the $[4,6]^+$ assignment with its higher collectivity. The falling Q_t values above this spin confirm the band termination at the 30^+ state, the highest spin state observed experimentally.

The Q_t value of the 1541 keV $24^+ \rightarrow 22_2^+$ transition is similar to that of the yrast $26^+ \rightarrow 24^+$ transition and much larger than that of the 2088 keV yrast $24^+ \rightarrow 22^+$ decay. This fact and the position of the 22_2^+ state in the energy graph in the middle panel of Fig. 8 suggest that the 22_2^+ and yrast 24^+ states belong to the $[4,6]^+$ configuration. This supports the second possibility mentioned above, that the yrast 22^+ state is the last observed member of the $[2,6]^+$ configuration and the 2088 keV yrast $24^+ \rightarrow 22^+$ transition is an interband decay. The level scheme in Fig. 5 represents this interpretation. It is less clear whether either the 20_2^+ or 20_3^+ states belong to the $[4,6]^+$ configuration, but the high energies and low Q_t values for their decays to the yrast 18^+ state show that these are interband transitions. Theoretical Q_t values for the configurations $[2,6]^+$ and $[4,6]^+$ are graphed in the top panel of Fig. 8. The slopes of these theoretical curves agree rather well with the experimental ones as the fully aligned state is approached. Since the CNS calculations do not include pairing, making them less reliable at low spins, theoretical Q_t values are graphed only for moderate to high spins.

The Q_t values in band 4 are generally stronger than those in band 2 although the moments of inertia in band 2 are larger than those in band 4 (middle panel of Fig. 7). Interband transitions indicate a degree of mixing between bands 2 and 4. The Q_t values of these interband transitions (not graphed) are generally smaller than the intraband ones.

The evolution of shape in the CNS calculations is shown in Fig. 9. Both the $[2,6]^+$ and $[4,6]^+$ configurations start out from triaxial shapes of moderate deformation and evolve towards much less deformed shapes. The $[2,6]^+$ configuration becomes fully aligned at a nearly spherical shape on the noncollective axis, while the $[4,6]^+$ one terminates at a slightly deformed triaxial shape.

The magnetic dipole transition strengths $B(M1)$ between band 2 and its signature partner (not numbered) are graphed in the upper part of Fig. 10. The strong alternating pattern was reported previously [7]. Such patterns have been seen in a number of $A \approx 80$ nuclei and have been explained both in the interacting Boson-Fermion approximation [7] and in the

TABLE III. Level energies, initial spin, γ-ray energies, branching ratios, electric quadrupole transition strengths, and electric quadrupole transition moments in ^{86}Zr. Energies and spins were taken from Ref. [2]. Branching ratios were deduced from the data of Ref. [2].

E_x (keV)	I_i^π	E_γ (keV)	B (%)	$B(E2)$ (W.u.)	$\lvert Q_t \rvert$ (e b)
			$\pi = +$		
20532	30^+	2469	100	>5.0	>0.55
18063	28^+	2013	100	$15.7^{+6.3}_{-3.5}$	$0.99^{+0.18}_{-0.12}$
16050	26^+	1903	100	$36.3^{+36.3}_{-12.1}$	$1.51^{+0.63}_{-0.28}$
14147	24^+	2088	43(2)	$4.9^{+1.8}_{-1.2}$	$0.56^{+0.10}_{-0.08}$
		1541	57(2)	$29.7^{+11.0}_{-6.9}$	$1.37^{+0.23}_{-0.17}$
12606	22^+	1431	56(3)	$18.8^{+12.6}_{-5.9}$	$1.09^{+0.32}_{-0.19}$
		1688	44(3)	$6.4^{+4.5}_{-2.2}$	$0.64^{+0.20}_{-0.12}$
12059	22^+	1917	100	$15.5^{+12.4}_{-4.7}$	$0.99^{+0.34}_{-0.17}$
11175	20^+	2526	100	$5.0^{+12.5}_{-2.1}$	$0.57^{+0.49}_{-0.13}$
10918	20^+	2269	68(3)	$2.7^{+3.2}_{-1.1}$	$0.42^{+0.20}_{-0.09}$
10142	20^+	1493	87(2)	$22.4^{+2.8}_{-2.4}$	$1.19^{+0.08}_{-0.06}$
9890	19^+	1643	70(2)	$6.4^{+1.0}_{-0.8}$	$0.64^{+0.05}_{-0.05}$
9652	(18^+)	1508	100	>7.0	>0.66
8649	18^+	1254	54(1)	$21.7^{+2.0}_{-1.8}$	$1.18^{+0.05}_{-0.05}$
8247	17^+	1233	35(2)	$15.9^{+2.3}_{-2.0}$	$1.01^{+0.07}_{-0.06}$
8144	16^+	1392	100	$24.7^{+16.0}_{-7.0}$	$1.26^{+0.36}_{-0.19}$
7953	16^+	1634	42(2)	$1.7^{+0.8}_{-0.4}$	$0.33^{+0.07}_{-0.05}$
		1201	12(3)	$2.3^{+1.5}_{-1.1}$	$0.38^{+0.12}_{-0.10}$
		1159	8(4)	$1.8^{+1.6}_{-1.3}$	$0.34^{+0.15}_{-0.14}$
7395	16^+	1075	30(2)	$15.7^{+4.2}_{-3.3}$	$1.01^{+0.13}_{-0.11}$
6752	14^+	1229	69(3)	$19.8^{+5.5}_{-3.8}$	$1.13^{+0.15}_{-0.11}$
		1357	18(3)	$3.1^{+1.2}_{-1.0}$	$0.45^{+0.09}_{-0.08}$
6320	14^+	925	82(2)	$5.8^{+0.8}_{-0.7}$	$0.62^{+0.04}_{-0.04}$
		797	18(2)	$2.7^{+0.7}_{-0.5}$	$0.42^{+0.05}_{-0.04}$
5523	12^+	1105	52(2)	$23.3^{+11.2}_{-6.4}$	$1.24^{+0.27}_{-0.17}$
		1198	48(2)	$14.4^{+6.9}_{-3.9}$	$0.97^{+0.22}_{-0.14}$
5395	12^+	1070	66(1)	$4.5^{+1.4}_{-0.9}$	$0.54^{+0.09}_{-0.05}$
		978	34(1)	$3.6^{+1.2}_{-0.8}$	$0.49^{+0.08}_{-0.06}$
4418	10^+	886	87(2)	>3.8	>0.50
		1120	13(2)	>0.1	>0.10
4325	10^+	1027	100	$10.2^{+1.8}_{-1.4}$	$0.83^{+0.08}_{-0.06}$
3532	8^+	862	14(2)	$2.3^{+0.9}_{-0.7}$	$0.39^{+0.08}_{-0.06}$
3298	8^+	628	100	$5.5^{+0.7}_{-0.6}$	$0.62^{+0.04}_{-0.03}$
2670	6^+	1003	100	$3.0^{+1.3}_{-0.7}$	$0.46^{+0.09}_{-0.06}$
1667	4^+	915	100	$6.9^{+3.2}_{-1.6}$	$0.74^{+0.16}_{-0.10}$
752	2^+	752	100	$13.9^{+2.4}_{-1.8}$	$1.26^{+0.10}_{-0.08}$
			$\pi = -$		
16616	27^-	2240	100	>3.7	>0.49
14376	25^-	1634	86(2)	$6.8^{+1.6}_{-1.1}$	$0.66^{+0.07}_{-0.06}$
12742	23^-	1509	61(2)	$11.8^{+4.3}_{-2.7}$	$0.86^{+0.15}_{-0.10}$
12361	22^-	1564	54(1)	$8.0^{+1.2}_{-1.0}$	$0.71^{+0.06}_{-0.04}$
11758	(21^-)	1875	50(2)	$4.9^{+6.4}_{-2.0}$	$0.56^{+0.29}_{-0.12}$
11233	21^-	1352	50(2)	$11.8^{+3.0}_{-2.2}$	$0.86^{+0.11}_{-0.08}$
11178	(20^-)	1644	100	$9.1^{+28.6}_{-3.9}$	$0.76^{+0.79}_{-0.19}$
10796	20^-	1422	48(2)	$14.2^{+7.7}_{-4.2}$	$0.95^{+0.23}_{-0.15}$
10208	19^-	1632	33(3)	$2.2^{+0.8}_{-0.5}$	$0.37^{+0.07}_{-0.04}$
9881	19^-	1305	42(1)	$16.1^{+5.5}_{-3.5}$	$1.01^{+0.16}_{-0.11}$

TABLE III. (*Continued*).

E_x (keV)	I_i^π	E_γ (keV)	B (%)	$B(E2)$ (W.u.)	$\lvert Q_t \rvert$ (e b)
		1209	17(2)	$9.5^{+4.1}_{-2.9}$	$0.78^{+0.15}_{-0.13}$
9373	18^-	1160	29(3)	$10.6^{+6.6}_{-3.7}$	$0.82^{+0.24}_{-0.15}$
8576	17^-	1231	72(2)	$9.5^{+1.1}_{-0.9}$	$0.78^{+0.05}_{-0.04}$
7640	15^-	1301	100	>5.1	>0.57
7470	15^-	1237	12(2)	$1.6^{+0.8}_{-0.6}$	$0.32^{+0.08}_{-0.07}$
		1131	30(2)	$6.3^{+2.6}_{-1.7}$	$0.64^{+0.12}_{-0.09}$
		1008	58(2)	$21.7^{+8.6}_{-5.5}$	$1.19^{+0.22}_{-0.17}$
6233	13^-	999	92(2)	$5.5^{+1.2}_{-0.8}$	$0.60^{+0.06}_{-0.04}$
5975	12^-	908	24(2)	>7.0	>0.68
5389	11^-	959	100	$11.1^{+3.7}_{-2.2}$	$0.86^{+0.13}_{-0.09}$
5234	11^-	804	15(2)	$0.9^{+0.8}_{-0.4}$	$0.24^{+0.10}_{-0.05}$
		597	20(1)	$5.3^{+4.5}_{-1.9}$	$0.59^{+0.22}_{-0.11}$
		537	9(2)	$4.0^{+4.1}_{-2.1}$	$0.52^{+0.23}_{-0.15}$
4430	9^-	1006	97(2)	$3.1^{+1.3}_{-0.7}$	$0.46^{+0.10}_{-0.08}$
		783	3(2)	$0.3^{+0.3}_{-0.2}$	$0.15^{+0.07}_{-0.06}$
3647	7^-	630	60(3)	>21.9	>1.24
3424	7^-	718	100	$17.7^{+3.3}_{-2.4}$	$1.12^{+0.10}_{-0.08}$

[a]For reference, 1 W.u. = 22.55 e^2 fm^4.

particle-rotor coupling model [21]. Basically, the transitions from odd-to-even spin have strong $B(M1)$ values because they involve only a spin flip by the unpaired particle(s), while the weak even-to-odd spin transitions require a change of the core rotation (or boson number).

TABLE IV. Level energies, initial spin, γ-ray energies, branching ratios, and magnetic dipole transition strengths in the positive-parity bands.

E_x (keV)	I_i^π	E_γ (keV)	B (%)	$B(M1)^a$ (μ_N^2)
10918	20^+	776	32(3)	$0.26^{+0.26}_{-0.12}$
10142	20^+	251	13(2)	$2.47^{+0.67}_{-0.62}$
9890	19^+	1242	30(2)	$0.027^{+0.005}_{-0.005}$
8649	18^+	401	46(1)	$1.40^{+0.13}_{-0.12}$
8247	17^+	852	49(2)	$0.16^{+0.02}_{-0.02}$
		294	16(2)	$1.28^{+0.31}_{-0.28}$
7953	16^+	939	38(2)	$0.034^{+0.009}_{-0.009}$
7395	16^+	381	70(2)	$1.51^{+0.24}_{-0.24}$
7014	15^+	694	91(2)	$0.27^{+0.07}_{-0.05}$
		220	9(2)	$0.83^{+0.38}_{-0.33}$
6752	14^+	432	13(3)	$0.20^{+0.10}_{-0.08}$
6286	13^+	891	100	$0.10^{+0.03}_{-0.02}$
3532	8^+	234	86(2)	$0.82^{+0.23}_{-0.15}$

[a]For reference, 1 W.u. = 1.79μ_N^2.

B. Negative-parity bands

Somewhat less structure change appears in the graphs of spin and moment of inertia for the negative-parity states

TABLE V. Level energies, initial spin, γ-ray energies, branching ratios, and magnetic dipole transition strengths in the negative-parity bands.

E_x (keV)	I_i^π	E_γ (keV)	B (%)	$B(M1)^a$ (μ_N^2)
14376	25^-	214	14(2)	$1.94^{+0.85}_{-0.79}$
12742	23^-	381	39(2)	$1.68^{+0.65}_{-0.42}$
12361	22^-	603	46(1)	$0.46^{+0.07}_{-0.06}$
11758	(21^-)	580	50(2)	$0.91^{+0.75}_{-0.37}$
11233	21^-	437	50(2)	$1.01^{+0.21}_{-0.19}$
10796	20^-	588	52(2)	$0.70^{+0.37}_{-0.20}$
10208	19^-	834	67(3)	$0.14^{+0.03}_{-0.03}$
9881	19^-	508	35(2)	$0.61^{+0.19}_{-0.15}$
		348	6(4)	$0.33^{+0.30}_{-0.15}$
9533	(18^-)	862	100	$0.18^{+0.07}_{-0.06}$
9373	18^-	797	71(3)	$0.17^{+0.06}_{-0.05}$
8576	17^-	363	28(2)	$0.34^{+0.05}_{-0.05}$
8213	16^-	742	100	$0.44^{+0.10}_{-0.08}$
6233	13^-	258	8(2)	$0.044^{+0.097}_{-0.031}$
5975	12^-	741	76(2)	>0.053
5234	11^-	167	2(1)	$0.014^{+0.017}_{-0.011}$
3647	7^-	223	40(3)	>0.21
3017	5^-	311	100	>0.095

[a]For reference, 1 W.u. = 1.79μ_N^2.

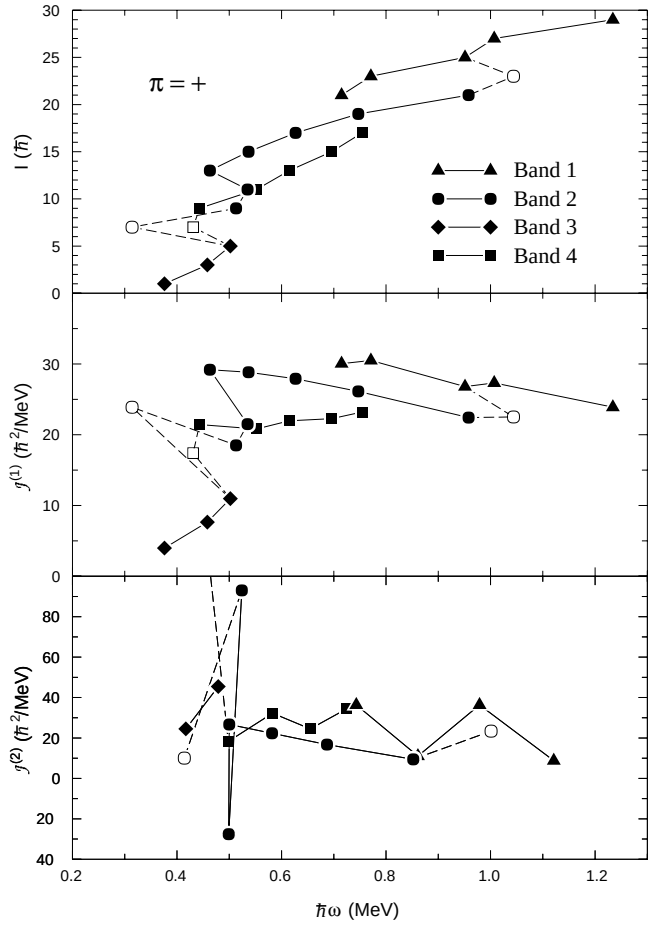

FIG. 7. Top: Spin I vs angular frequency $\hbar\omega$ for the positive-parity bands. Middle: Kinematic moment of inertia $J^{(1)}$ vs $\hbar\omega$. Bottom: Dynamic moment of inertia $J^{(2)}$ vs $\hbar\omega$. Open symbols and dashed lines in the figure indicate interband transitions or states.

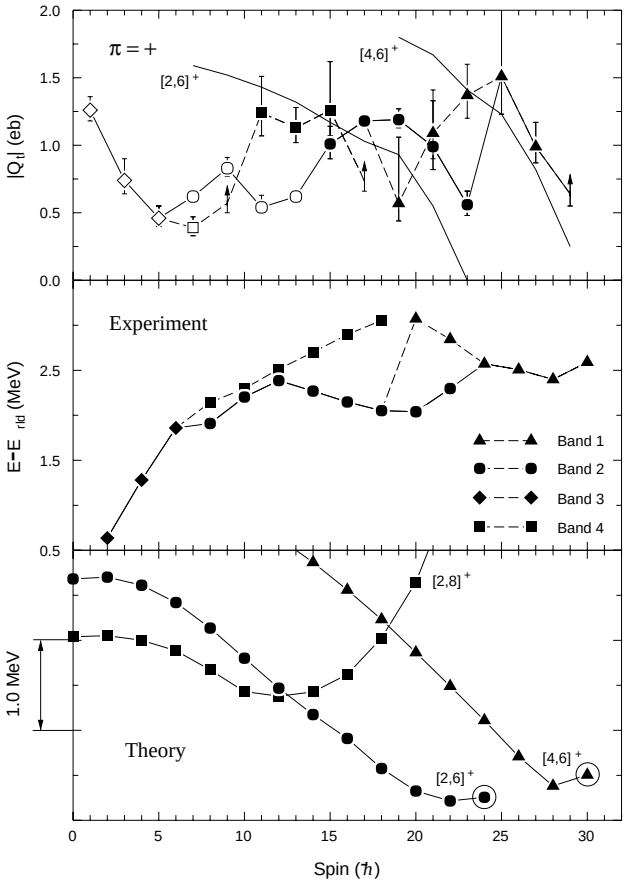

FIG. 8. Top: The electric transition quadrupole moments $|Q_t|$ vs spin I for the positive-parity bands 1, 2, 3, and 4. Filled symbols indicate values calculated from lifetimes measured in this work and open symbols represent values calculated from previously measured lifetimes. Arrows indicate lower-limit values. The solid line follows the yrast sequence. Two theoretical $|Q_t|$ lines are graphed for the $[2,6]^+$ and $[4,6]^+$ configurations. Middle: Experimental level energies minus a rotating liquid drop reference $[(0.0193\ \text{MeV})I(I-1)]$. Bottom: Calculated energies relative to the rotating liquid drop for configurations likely to correspond to observed bands.

shown in Fig. 11. Positive g factors for the yrast 5^-, 7^-, and 9^- states in band 8 rule out pure neutron configurations, but are low enough to suggest that mixed proton and neutron aligned configurations are most likely [9]. However, nothing is known about the g factors of the higher-lying negative-parity states.

In Fig. 11, a peak in band 5 is observed in the $J^{(2)}$ graph (bottom) corresponding possibly to a structural change at ≈ 0.6 MeV. A change in slope can also be seen at this angular frequency in the other panels of this figure. This change occurs where an interband $E2$ decay appears between bands 5 and 8, as can be seen in the level scheme and as an open circle in the upper panels of Fig. 11.

The experimental energies in band 5 above this change (middle panel of Fig. 12) agree rather well with the CNS predictions for the $[3,6]^-$ configuration (bottom panel of Fig. 12). The $[3,6]^-$ configuration terminates at the fully aligned 27^- state, and the 27^- state is the last one observed in experimental band 5. For band 6 two possible configurations ($[3,6]_a^+$ and $[3,6]^+$) are plotted, since it is not immediately clear which one is the best candidate. The signature between the three protons in the $g_{9/2}$ and the three proton holes in the $p_{3/2}$ and $f_{5/2}$ shells is interchanged in $[3,6]_a^+$ relative to $[3,6]^+$. The $[3,6]_a^+$ configuration reproduces the big energy difference as seen in the middle panel and the signature splitting well, whereas the $[3,6]^+$ configuration lies lower in energy and the question arises why the latter configuration should not be favored over the former one. In any case, the relative displacement in the I versus $\hbar\omega$ graph between the bands, seen in the positive-parity bands, does not appear here, indicating that the number of $g_{9/2}$ particles in these bands is approximately constant.

The transition quadrupole moments for the negative-parity states (top panel of Fig. 12) are somewhat smaller than those among the positive-parity states, averaging about 0.75 e b. They are also generally more constant at higher

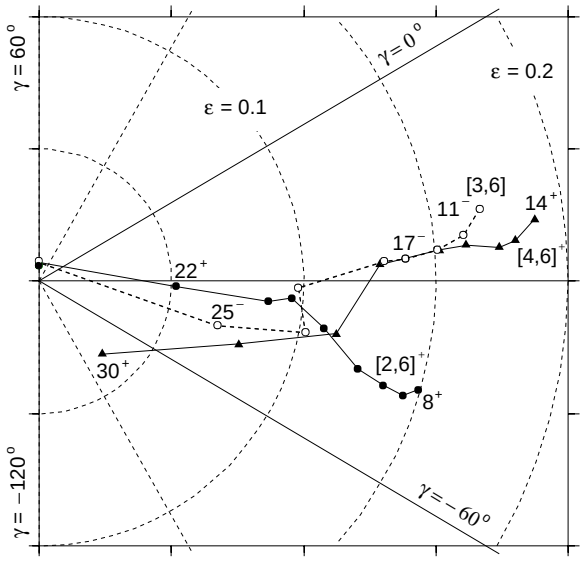

FIG. 9. Shape parameters ϵ and γ (Lund convention) calculated in the CNS model as a function of spin for three configurations which appear to represent experimentally observed bands.

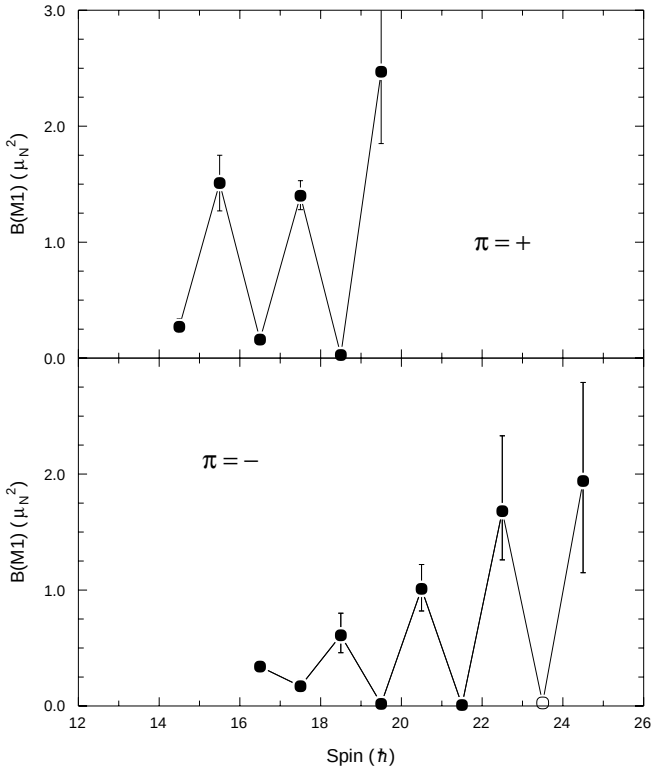

FIG. 10. The magnetic dipole transition strengths $B(M1)$ vs spin between band 2 and its signature partner (top) and bands 5 and 6 (bottom). The open symbol represents a $B(M1)$ value estimated by assuming the mean lifetime for the 14 162 keV negative-parity level (band 6) is equal to that of the 14 376 keV negative-parity level (band 5).

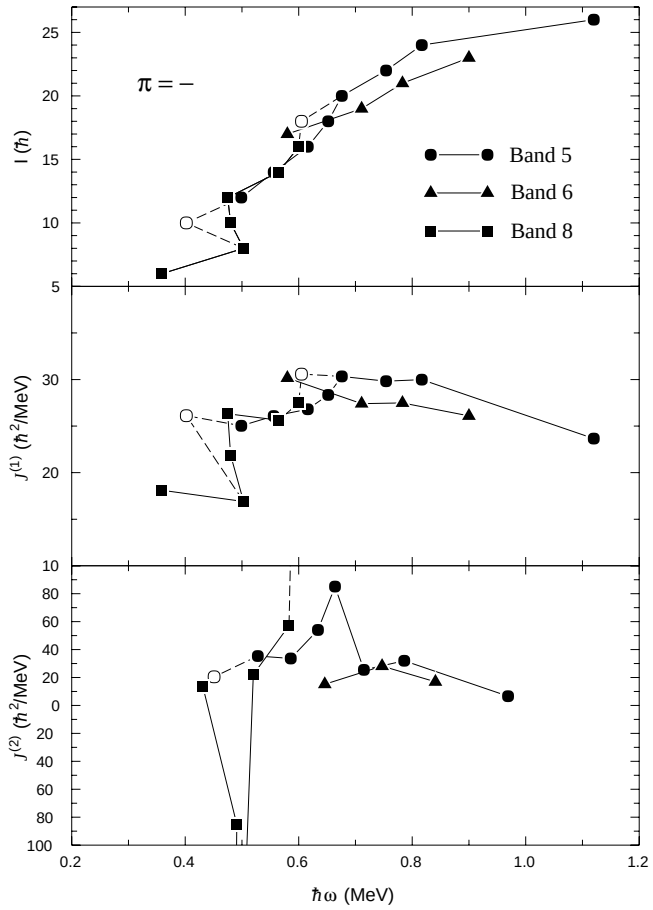

FIG. 11. Top: Spin I vs angular frequency $\hbar\omega$ for the negative-parity bands. Middle: Kinematic moment of inertia $J^{(1)}$ vs $\hbar\omega$. Bottom: Dynamic moment of inertia $J^{(2)}$ vs $\hbar\omega$. Open symbols and dashed lines in the figure indicate interband transitions or states.

spins than those in the positive-parity bands. The last four data points in band 5 approaching the state at 27^- decrease relatively steadily but not as rapidly as their positive-parity counterparts, indicating a smoother band termination. The theoretical Q_t line graphed for the $[3,6]^-$ configuration reproduces this fall off, but is somewhat steeper. As seen in Fig. 9, the shape calculated for the $[3,6]^-$ configuration starts out with moderate triaxial deformation and terminates at a fully aligned, nearly spherical shape.

From the lifetime measurements an alternating pattern in the $B(M1)$ strengths was revealed between bands 5 and 6, as shown in the lower part of Fig. 10. The alternations appear to increase with spin and extend over a wider range than the positive-parity sequence. The increase in the amplitude of the $B(M1)$ alternations parallels the increase in signature splitting with spin seen in the middle panel of Fig. 12.

VI. SUMMARY

High-spin states in ^{86}Zr were produced in the fusion evaporation reaction ^{58}Ni(^{32}S,4p) at 135 MeV. Multi-γ co-

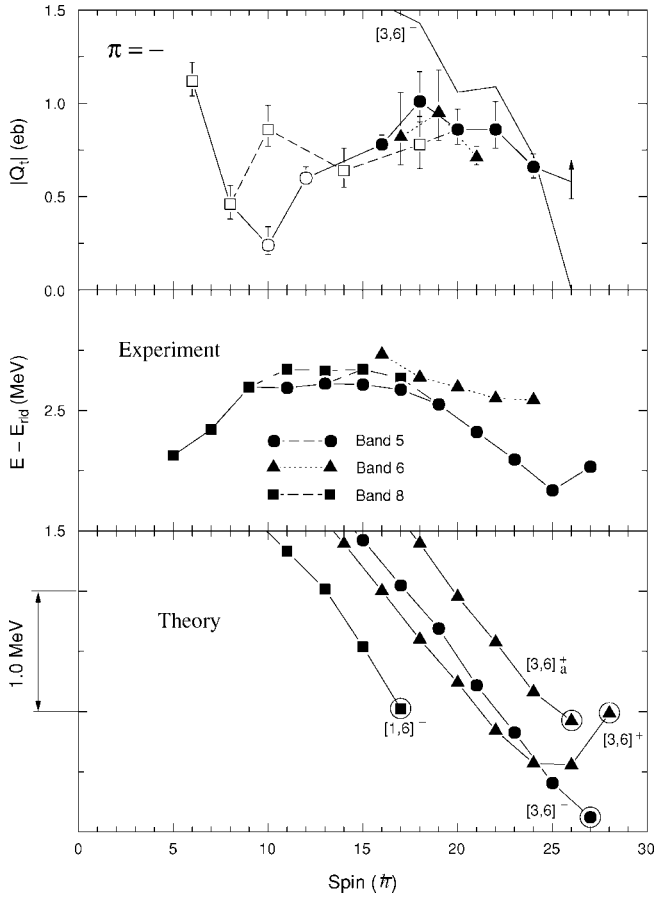

FIG. 12. Top: The electric transition quadrupole moments $|Q_t|$ vs spin I for the negative-parity bands 5, 6, and 8. Filled symbols indicate values calculated from lifetimes measured in this work and open symbols represent values calculated from previously measured lifetimes. The arrow indicates a lower-limit value. The solid line follows the negative-parity yrast sequence. A theoretical $|Q_t|$ line is graphed for the $[3,6]^-$ configuration. Middle: Experimental level energies minus a rotating liquid drop reference $[(0.0193\ \mathrm{MeV})I(I-1)]$. Bottom: Calculated energies relative to the rotating liquid drop for configurations likely to correspond to observed bands.

incidences and evaporated charged particles were detected with the full GAMMASPHERE array and the MICROBALL. Due to the thick target backing, lifetimes of 36 high-spin states in ^{86}Zr could be measured with the Doppler-shift attenuation method. To extract clean line shapes, triple-γ coincidences and charged particle gates were used. Side-feeding times averaged about 30% of the effective lifetime of the state immediately above the transition of interest. Whenever possible line shapes were extracted using gates set above the transition of interest to eliminate the contribution of side feeding. Transition quadrupole moments Q_t were calculated from the lifetimes and range from 0.3 to 1.5 e b in the positive-parity bands. The negative-parity bands show Q_t values from about 0.25 to 1.2 e b. The negative-parity Q_t values for the high-spin states show far less variation than the positive-parity states. The Q_t values confirm the band termination at the 30^+ state and agree with the terminations at the 24^+ and 27^- states which were previously suggested by the level energies. In addition, the Q_t values imply that the only observed 24^+ level belongs to the more deformed $[4,6]^+$ configuration and is not the terminating state of the $[2,6]^+$ configuration.

Strong alternating magnetic dipole transition strengths $B(M1)$ were observed between the yrast odd and even spin negative-parity states, as had been previously reported among some positive-parity states.

ACKNOWLEDGMENTS

This work was supported in part by the National Science Foundation under Grant Nos. PHY-9523974 and PHY-9970991 (FSU) and in part by the U.S. Department of Energy under Contract Nos. DE-AC05-76OR00033 (UNISOR), DE-AC05-96OR22464 (ORNL), DE-FG05-88ER40406 (WU), and DE-AC03-76SF00098 (LBNL). F.C. acknowledges support from Colciencias (Bogotá), Contract No. 222-96.

[1] D.G. Sarantites, D.R. LaFosse, M. Devlin, F. Lerma, V.Q. Wood, J.X. Saladin, D.F. Winchell, C. Baktash, C.-H. Yu, P. Fallon, I.Y. Lee, A.O. Macchiavelli, R.W. MacLeod, A.V. Afanasjev, and I. Ragnarsson, Phys. Rev. C **57**, R1 (1998).

[2] J. Döring, Y.A. Akovali, C. Baktash, F.E. Durham, C.J. Gross, P.F. Hua, G.D. Johns, M. Korolija, D.R. LaFosse, I.Y. Lee, A.O. Macchiavelli, W. Rathbun, D.G. Sarantites, D.W. Stracener, G.Z. Solomon, S.L. Tabor, A. Vander Molen, A.V. Afanasjev, and I. Ragnarsson, Phys. Rev. C **61**, 034310 (2000).

[3] T. Bengtsson and I. Ragnarsson, Nucl. Phys. **A436**, 14 (1985).

[4] M. Avrigeanu, V. Avrigeanu, D. Bucurescu, G. Constantinescu, M. Ivascu, D. Pantelica, M. Tanase, and N.V. Zamfir, J. Phys. G **4**, 261 (1978).

[5] J. Hattula, S. Juutinen, H. Helppi, A. Pakkanen, M. Piiparinen, S. Elfström, and Th. Lindblad, Phys. Rev. C **28**, 1860 (1983).

[6] E.K. Warburton, C.J. Lister, J.W. Olness, P.E. Haustein, S.K. Saha, D.E. Alburger, J.A. Becker, R.A. Dewberry, and R.A. Naumann, Phys. Rev. C **31**, 1211 (1985).

[7] P. Chowdhury, C.J. Lister, D. Vretenar, Ch. Winter, V.P. Janzen, H.R. Andrews, D.J. Blumenthal, B. Crowell, T. Drake, P.J. Ennis, A. Galindo-Uribarri, D. Horn, J.K. Johansson, A. Omar, S. Pilotte, D. Prévost, D. Radford, J.C. Waddington, and D. Ward, Phys. Rev. Lett. **67**, 2950 (1991).

[8] M. Weiszflog, J. Billowes, J. Eberth, C.J. Gross, M.K. Kabadiyski, K.P. Lieb, T. Mylaeus, and D. Rudolph, Nucl. Phys. **A584**, 133 (1995).

[9] A.W. Mountford, T. Vass, G. Kumbartzki, L.A. Bernstein, N. Benczer-Koller, R. Tanczyn, C.J. Lister, P. Chowdhury, and S.J. Freeman, Phys. Rev. C **51**, 513 (1995).
[10] C. Teich, A. Jungclaus, V. Fischer, D. Kast, K.P. Lieb, C. Lingk, C. Ender, T. Härtlein, F. Köck, D. Schwalm, J. Billowes, J. Eberth, and H.G. Thomas, Phys. Rev. C **59**, 1943 (1999).
[11] R.A. Kaye, J.B. Adams, A. Hale, C. Smith, G.Z. Solomon, S.L. Tabor, G. García-Bermúdez, M.A. Cardona, A. Filevich, and L. Szybisz, Phys. Rev. C **57**, 2189 (1998).
[12] I.Y. Lee, Nucl. Phys. **A520**, 641c (1990).
[13] D.G. Sarantites, P.-F. Hua, M. Devlin, L.G. Sobotka, J. Elson, J.T. Hood, D.R. LaFosse, J.E. Sarantites, and M.R. Maier, Nucl. Instrum. Methods Phys. Res. A **381**, 418 (1996).
[14] M. Wiedeking, R.A. Kaye, G.Z. Solomon, S.L. Tabor, J. Döring, G.D. Johns, F. Cristancho, M. Devlin, F. Lerma, D.G. Sarantites, I.Y. Lee, and A.O. Macchiavelli, Phys. Rev. C **62**, 024316 (2000).
[15] E.F. Moore, P.D. Cottle, C.J. Gross, D.M. Headly, U.J. Hüttmeier, S.L. Tabor, and W. Nazarewicz, Phys. Rev. C **38**, 696 (1988).
[16] J.F. Ziegler, J.P. Biersack, and U. Littmark, *The Stopping and Range of Ions in Matter* (Pergamon, New York, 1985).
[17] See http://www.SRIM.org
[18] A.V. Afanasjev, D.B. Fossan, G.J. Lane, and I. Ragnarsson, Phys. Rep. **322**, 1 (1999).
[19] D. Galeriu, D. Bucurescu, and M. Ivascu, J. Phys. G **12**, 329 (1986).
[20] H. Sun, J. Döring, G.D. Johns, R.A. Kaye, G.Z. Solomon, S.L. Tabor, M. Devlin, D.R. LaFosse, F. Lerma, D.G. Sarantites, C. Baktash, D. Rudolph, C.-H. Yu, I.Y. Lee, A.O. Macchiavelli, I. Birriel, J.X. Saladin, D.F. Winchell, V.Q. Wood, and I. Ragnarsson, Phys. Rev. C **59**, 655 (1999).
[21] P.C. Womble, J. Döring, T. Glasmacher, J.W. Holcomb, G.D. Johns, T.D. Johnson, T.J. Petters, M.A. Riley, V.A. Wood, and S.L. Tabor, Phys. Rev. C **47**, 2546 (1993).